ARTICLE

Study of the Excited-State Proton-Transfer Reaction of 5-Cyano-2-naphthol in Sub- and Supercritical Water

I. Kobayashi, M. Terazima, and Y. Kimura*

Department of Chemistry, Graduate School of Science, Kyoto University, Kyoto 606-8502, Japan

Ⓢ *Supporting Information*

ABSTRACT: The excited-state proton-transfer (ESPT) reaction of 5-cyano-2-naphthol (5CN2) has been investigated in sub- and supercritical water using time-resolved fluorescence measurements. Under ambient conditions, a very fast decay of the fluorescence from the excited state of normal 5CN2 (ROH*) and a simultaneous increase of the fluorescence from the excited state of the anion species (RO⁻*) were observed, as reported previously. The very high ESPT rate was evaluated as 0.12 ps⁻¹. With increasing temperature at a constant pressure of 39.0 MPa, the proton transfer became slow. At 615 K and 39.0 MPa, another fluorescence from a new unknown chemical species appeared, which was assigned to the contact ion pair (CIP) of RO⁻* and the hydronium ion. With decreasing pressure at 664 K, the fluorescence from RO⁻* disappeared, and the fluorescence from ROH* and CIP was observed. At the very low density of supercritical water, only the fluorescence decay of ROH* was detected. The reaction dynamics was analyzed with the help of singular value decomposition and spectral decomposition using model functions. The ESPT rate was correlated with the solvent dielectric constant and/or the hydrogen-bonding ability.
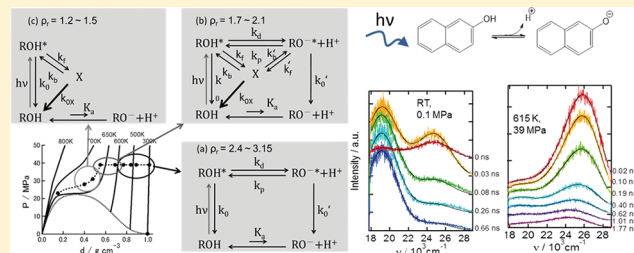
1. INTRODUCTION

Supercritical water (SCW) and supercritical alcohols have attracted much attention because of their unique properties and chemical applications.[1,2] The structure and properties of SCW and supercritical alcohols have been investigated by various spectroscopic methods such as nuclear magnetic resonance (NMR) spectrometry, X-ray scattering, and Raman spectroscopy.[3−13] The existence of hydrogen bonding between water molecules has been demonstrated under supercritical conditions, except in the extremely gas-like region.[7,14] It was found that the number of hydrogen bonds between water molecules is strongly dependent on temperature and density. From studies using molecular dynamics simulations, an almost-linear correlation was found between the dielectric constant and the average number of hydrogen bonds in SCW.[15]

On the other hand, there have been few studies on solute−solvent hydrogen bonding in protic supercritical fluids mainly because of experimental difficulties encountered at high temperature and high pressure. [The critical temperature (T_C) and pressure (P_C) of water are 647 K and 22.1 MPa, respectively.] Mostly the solvatochromic method has been used to probe the hydrogen bonding between solute and solvent.[16−25] Recently, our group developed a high-pressure and high-temperature optical cell available for various spectroscopic experiments and studied solute−solvent hydrogen bonding in SCW and supercritical alcohols using the Raman spectroscopic method.[26−31] In these works, the effects of solute−solvent hydrogen bonding on the NO_2 and NH_2 stretching vibrations of *p*-nitroaniline (pNA) and the CN stretching vibration of *p*-aminobenzonitrile were

revealed. However, the relation of the changes in solute−solvent hydrogen bonding with basic chemical reactions in SCW such as electron transfer and proton transfer is still not clear.

In this article, we report a study on the proton-transfer (PT) reaction in SCW. Because the PT process involves motion of the proton, the PT process is very sensitive to the degree of hydrogen bonding and also to the dielectric properties of the solvent. The question of how the PT rate changes in relation to solute−solvent hydrogen-bonding or the solvent dielectric properties of SCW with the variation of the density is quite interesting. However, only a few previous studies on the PT process in SCW have been reported. To the best of our knowledge, spectroscopic studies on the PT process in SCW were reported for the excited-state PT (ESPT) of 2-naphthol (2-NpOH) about 15 years ago.[32,33] In these reports, the ESPT process of 2-NpOH was investigated not only in water under sub- and supercritical conditions but also in acid and base aqueous solutions, using steady-state and time-resolved fluorescence spectroscopy. 2-NpOH shows dual fluorescence from the electronic excited states of both 2-NpOH* and the anion (2-NpO⁻*) after ESPT, and the ESPT can be followed by the time profile of the fluorescence. According to their studies, fluorescence from 2-NpO⁻* could not be detected above 423 K. On the other hand, in a basic solution of ammonia, fluorescence from 2-NpO⁻* was observed even at elevated temperature. They monitored the ESPT

kinetics mostly by monitoring the initial decay of fluorescence from 2-NpOH*. It was found that the isobaric PT rate exhibits Arrhenius-like behavior in acetic acid and borate aqueous solutions, whereas it shows a non-Arrhenius dependence in aqueous ammonia and pure water. The non-Arrhenius behavior was attributed to the loss of solvation of water at high temperature due to the structural change of water and the weakening of the polarity and hydrogen-boding ability. They also suggested the plausible existence of contact ion pairs $[2\text{-NpO}^-\cdots\text{H}^+]^*$ at elevated temperature, which might cause the rapid quenching of 2-NpO$^-$*.

In their studies, however, PT kinetics was not studied well in neutral water, as no fluorescence from 2-NpO$^-$* was detected above 423 K. In this work, we used 5-cyano-2-naphthol as a probe molecule, and studied the ESPT dynamics in sub- and supercritical water. Cyano-substituted naphthols such as 5-cyano-2-naphthol (5CN2), 8-cyano-2-naphthol (8CN2), and 5,8-dicyano-2-naphthol (DCN2) have been shown to have higher acidities in the electronic excited state.[34−50] The value of pK_a* (the acid dissociation constant in the excited state) of 5CN2 was reported as −0.75, which is much smaller than that of 2-NpOH (2.8).[36] Therefore, the ESPT process of 5CN2 is expected to be observed at higher temperature than that of 2-NpOH. The ESPT process of cyano-substituted naphthols has been extensively studied mainly by fluorescence measurements, as the emissions from the excited states in both neutral (ROH*) and anionic forms (RO$^-$*) are observable as in the case of 2-NpOH. According to previous studies, the fluorescence dynamics of RO$^-$* shows bimodal behavior: there is a very fast formation of the RO$^-$* from ROH* after the photoexcitation, and then successively slower decay occurs as a result of the recombination of RO$^-$* with the dissociated proton, as well as radiative and nonradiative decays. The decay of RO$^-$* fluorescence was not exponential but asymptotic in the form of $t^{-3/2}$.[36,37] This form was explained by introducing an "encounter complex" of RO$^-$* and proton and by assuming that the rate-limiting step of encounter complex formation is the diffusion process. The photoexcitation dynamics of 5CN2 was also studied under supersonic jet conditions by Knochenmuss et al.[51] They found that ESPT occurred with a threshold cluster size of three or four solvent molecules in ammonia clusters. On the other hand, in water clusters, ESPT occurred with the threshold cluster size from 8 to 10, and no ESPT occurred in methanol and dimethyl sulfoxide clusters. How the ESPT dynamics will appear in SCW as the number of water molecules around 5CN2 changes is an interesting issue.

In the following section, we explain the experimental details, including sample preparation, high-pressure and high-temperature equipment, and methods for time-resolved fluorescence measurements. In section 3, the experimental results and analysis are presented. Finally, the evaluated ESPT rate is discussed in terms of the hydrogen bonding between water molecules.

2. EXPERIMENTAL SECTION

2.1. Materials. 5-Cyano-2-naphthol (5CN2) was synthesized from 6-methoxy-1-tetralone following the procedure in the literature[34,52] and purified by sublimation. Water purified by distillation was used for the experiments.

2.2. Fluorescence and Absorption Measurement at High Temperatures and Pressures. Two different methods were employed for the time-resolved fluorescence detections: a streak camera (Hamamatsu, C4334) method for all experimental

conditions and an optical Kerr gate method for the aqueous solution under ambient conditions. The experimental setups for these systems were almost the same as described before,[53] except for the excitation wavelength and the sample cell. In this study, the third-harmonic pulse (267 nm) produced by a regenerative amplifier of a Ti:sapphire laser was employed for the excitation. The calibrations of the wavelength, color sensitivity, and time delay due to group-velocity dispersion for each system were performed as reported previously.[53]

For the measurements under sub- and supercritical conditions of water, a specially designed high-pressure and high-temperature optical cell was used. The details of the optical cell and high-pressure system are described elsewhere.[26,29] Briefly, the cell was made of Hasteroy C and equipped with 2-mm-thick sapphire windows, and the optical path length was ca. 5 mm. The temperature of the cell was regulated with an accuracy of ca. ±1 K by a sheathed heater wounded around the cell and a thermocouple directly inserted into the sample chamber. The sample solution was flowed into the cell at a rate of 1.0 cm^3 min^{-1} using an high-performance liquid chromatography pump (JASCO, PU-2080plus). The pressure of the fluid was controlled by a back-pressure regulator (JASCO, 880-81) with an accuracy of about ±0.3 MPa. The concentration of the sample solution was ca. 3×10^{-4} M, nearly saturated in water.
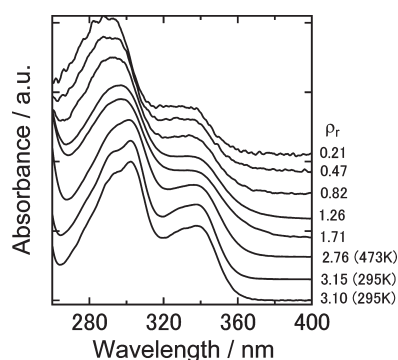
The absorption spectra under sub- and supercritical conditions of water were measured using a deuterium lamp as the light source, and the transmission intensity of the light after passing through the optical cell flowing pure water or the sample solution was successively measured by a multichannel detector (StellarNet, EPP2000C). The absorption and steady-state fluorescence spectra under ambient conditions were measured with commercial spectrometers (Shimadzu UV-2500PC and JASCO FP-6500, respectively) using a quartz cell with a 1-cm optical path length.

Absorption measurements were performed along the 39.0 MPa isobar between room temperature (room temperature, 295 K) and 664 K (corresponding density region is $\rho_r = 3.15 − 1.72$) and along the 664 K isotherm between 39.0 and 15.1 MPa ($\rho_r = 1.72 − 0.21$), where ρ_r is the reduced density relative to the critical density of water (322 kg m^{-3}). Time-resolved fluorescence experiments were performed along the 39.0 MPa isobar between room temperature and 664 K ($\rho_r = 3.15 − 1.72$) and along the 664 K isotherm between 39.0 and 22.6 MPa ($\rho_r = 1.72 − 0.47$). The density of water was calculated using an equation of state.[54]

3. RESULTS AND ANALYSIS

3.1. Absorption Spectra in Sub- and Supercritical Water. Figure 1 shows absorption spectra of 5CN2 in water at various pressures and temperatures. The spectral shapes are similar to one another under all conditions, although the relative intensity of the peak around 300 nm to that around 330 nm changes with the temperature and the pressure. It has been reported that the pK_a value of 5CN2 in the ground state is 8.75 and that 5CN2 in water exists in the neutral (ROH) form in the ground state.[36] The similarity of the absorption spectra in water under various conditions indicates that 5CN2 in the electronic ground state exists in the ROH form under all conditions studied here. The shape and the absorbance did not change during fluorescence measurements described below. This fact indicates that 5CN2 is chemically stable under the flow conditions (1 cm^3 min^{-1}) of our experiments even in high-temperature and high-pressure water.

1044

dx.doi.org/10.1021/jp2097422 |J. Phys. Chem. B 2012, 116, 1043–1052

Figure 1. Absorption spectra of 5CN2 in water under sub- and supercritical conditions. The spectra are normalized at the peak position around 300 nm and shown with different vertical offsets for clarity. The states of reduced densities $\rho_r = 0.21-1.72$ correspond to 15–39 MPa, respectively, at 664 K. The states with $\rho_r = 2.76$ and 3.15 correspond to 39 MPa at 473 and room temperature (295 K), respectively. The state with $\rho_r = 3.10$ corresponds to ambient conditions (0.1 MPa and 295 K).

3.2. Time-Resolved Fluorescence Spectra in Sub- and Supercritical Water.

3.2.1. Overview. Figure 2 shows time-resolved fluorescence spectra at various temperatures and pressures against the wavenumber. The time dependence of the fluorescence spectrum of 5CN2 was significantly dependent on the temperature and the pressure of water. Because 5CN2 exists in the ROH form in the ground state even under supercritical conditions, the photoexcitation of ROH initially produces ROH*. The fluorescence spectra under ambient conditions (Figure 2a) showed a rapid PT process from ROH* (fluorescence around 25000 cm^{-1}) to water, which resulted in the formation of RO$^-$* (fluorescence around 19000 cm^{-1}).[36] Because the time resolution of the streak camera was poor, the fluorescence from RO$^-$* was also apparent even at time zero (0 ns) in Figure 2a. At 519 K and 39 MPa (Figure 2b), the PT process became slow, as indicated by the relatively slow decay of ROH* fluorescence. At 615 K and 39 MPa (Figure 2c), a weak peak was observed around 19000 cm^{-1} nm 0.4 ns after photoexcitation that was assumed to be the emission from RO$^-$*. Simultaneously, the emission peak on the higher-wavenumber side was shifted from the initial value (26000 cm^{-1}) to 24000 cm^{-1}. In the longer time region, only a single fluorescence band centered on 24000 cm^{-1} decayed. This new emission band was also apparent in the fluorescence data at lower density (Figure 2d) at 664 K and 28 MPa, where no RO$^-$* emission was observed. One plausible interpretation of the apparent fluorescence peak shift in Figure 2c,d is due to the solvation dynamics of ROH*. However, the solvation dynamics of water is very fast (on the order of a few picoseconds),[55] and that of SCW in the relatively higher density region around $\rho_r \approx 2$ is also expected to be of similar order. As will be shown later, the spectral change at the higher-wavenumber side can be explained by relative intensity changes of two fluorescence bands originating from two different species; that is, the chemical species for the emission around 24000 cm^{-1} should be different from ROH* and RO$^-$*. Hereafter, we denote this third species as X.

To extract the number of species which contributed to the time-resolved spectra, singular value decomposition (SVD) analysis was applied to the time-resolved spectra. In the SVD analysis, the time-resolved spectra are decomposed into spectral components, and their time profiles are weighted by their
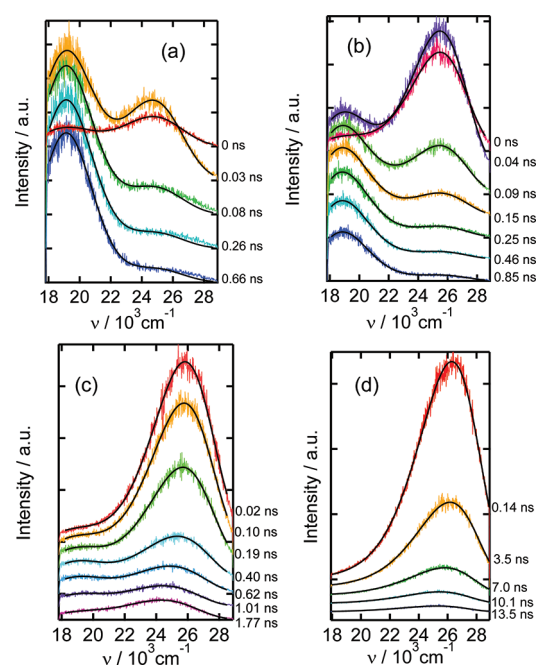

Figure 2. Time-resolved fluorescence spectra under typical conditions: (a) ambient conditions ($\rho_r = 3.10$), (b) 519 K and 39 MPa ($\rho_r = 2.60$), (c) 615 K and 39 MPa ($\rho_r = 2.13$), and (d) 664 K and 28 MPa ($\rho_r = 1.26$). Each spectrum at a different delay time is shown with a different vertical offset for clarity. The results of the spectral fitting using multi-log−normal functions are also shown as solid lines.

singular values (SVs).[56] The spectral components that have large singular values are considered to be real components, and other components are disregarded as noise. The spectral components obtained by the SVD analysis for typical experimental conditions are given in Figure S1 (Supporting Information). For example, the SV of the third component in Figure S1A (Supporting Information) is much smaller than the largest one, and its spectrum is very noisy for the data at room temperature and 0.1 MPa. In this case, we concluded that only two components predominantly contribute to the fluorescence spectra. Using a similar criterion, the numbers of the spectral components under various conditions were determined as follows: three for the data at 615 K and 39 MPa, one for the data at 664 K and 21 MPa, and two for the data under the other experimental conditions in this study. Because the spectral components obtained by the SVD analysis can be a linear combination of the spectral components of "real" chemical species, reconstruction of the spectrum from the spectra obtained by the SVD analysis is required. Because there are numerous possibilities for linear combinations of the SVD spectra, we took a rather ad hoc method; that is, we tried to simulate the spectrum at each delay time by a combination of log−normal functions, using the same number of log−normal functions as obtained by SVD analysis

$$I_{fl}(t,\nu) = \sum_j h_j(t)$$

$$\times \begin{cases} \exp\left[-\ln(2)\{\ln[1 + 2\gamma_j(\nu - \nu_{Pj})/\Delta_j]/\gamma_j\}^2\right] & 2\gamma_j(\nu - \nu_{Pj})/\Delta_j > -1 \\ 0 & 2\gamma_j(\nu - \nu_{Pj})/\Delta_j \leq -1 \end{cases}$$

$$(1)$$

where $I_{fl}(t,\nu)$ is the fluorescence intensity at the delay time t, j is the index for the spectral components, $h_j(t)$ is the intensity factor,
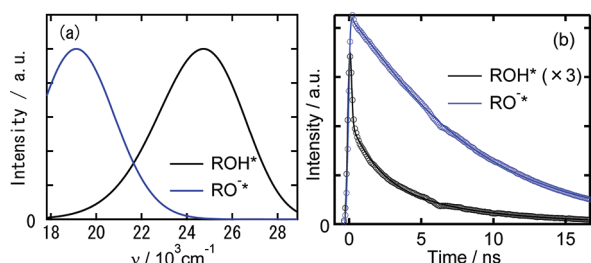
Figure 3. (a) Spectral components and (b) their time profiles under ambient conditions obtained by a fit to two log−normal functions. In panel b, the circles represent the obtained time profiles, and the solid lines represent the fitting curves to the time profiles obtained by the convolution of the response function.

Scheme 1. Experimental Conditions and Phase Diagram of Water and Proposed Reaction Schemes of 5CN2 under Different Thermodynamic Conditions
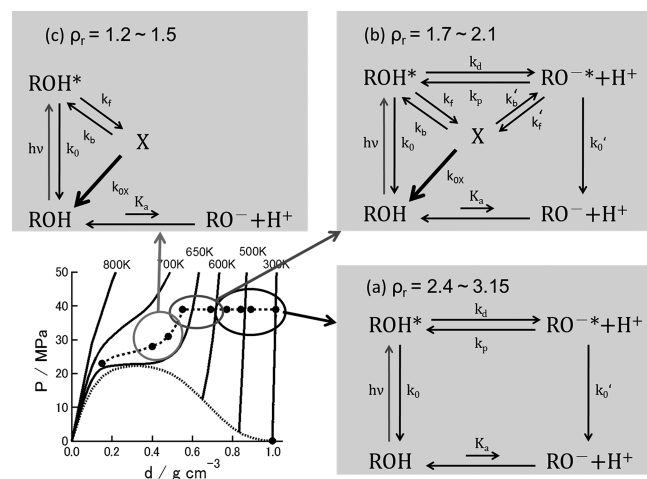
ν_{pj} is the peak position, γ_j is the asymmetric parameter, and Δ_j is the bandwidth parameter. We assumed that only the intensity factor is dependent on time t. In the following sections, reconstruction of the spectral components is presented.

3.2.2. Fluorescence Dynamics from Room Temperature to 567 K ($\rho_r = 3.15−2.40$). At room temperature under atmospheric pressure, two components were suggested to exist from the SVD analysis. This number is consistent with the conclusions of previous studies, and these chemical species were attributed to ROH* and RO⁻*.[37] The spectrum at each delay time was simulated by the sum of two log−normal functions as follows: First, the fluorescence spectrum at the longer delay time (ca. 17 ns) was simulated by a single log−normal function to obtain the parameters (ν_P, γ, and Δ in eq 1) for RO⁻*. Then, the fluorescence spectrum at a very early delay (ca. 0.1 ns) was simulated by the sum of two log−normal functions to obtain the parameters for ROH*, with the parameters for RO⁻* fixed. Using the parameters determined for ROH* and RO⁻*, the spectrum at each delay time was simulated by the sum of these two log−normal functions with different intensities. Figure 3 shows the spectral components and their time profiles. The fitting results for the time-resolved spectra using these spectral species are given by the solid black lines in Figure 2a. The spectra calculated in the above way reproduced the observed time-resolved spectra fairly well.

According to the reaction scheme shown in Scheme 1(a),[36] the rate equations are given by

$$\frac{d}{dt}[ROH^*] = -(k_d + k_0)[ROH^*] + k_p[RO^-*][H^+] \quad (2)$$

$$\frac{d}{dt}[RO^-*] = -(k_p[H^+] + k_0')[RO^-*] + k_d[ROH^*] \quad (3)$$

Here k_0 and k_0' represent the decay (radiative and nonradiative) rate constants of ROH* and RO⁻*, respectively. Assuming that k_0 and k_0' are much slower than the PT reaction, that the proton concentration is time-independent, and that the initial concentration of RO⁻* ($[RO^-*]_0$) is equal to zero, these equations can be approximately solved to give[57]

$$[ROH^*] = [ROH^*]_0 \frac{k_d}{k_1} \left\{ \exp(-k_1 t) + \frac{k_p[H^+]}{k_d} \exp(-k_S t) \right\} \quad (4)$$

$$[RO^-*] = [ROH^*]_0 \frac{k_d}{k_1}[-\exp(-k_1 t) + \exp(-k_S t)] \quad (5)$$

where

$$k_1 = k_p[H^+] + k_d \quad (6)$$

$$k_S = \frac{k_0' k_d + k_0 k_p[H^+]}{k_d + k_p[H^+]} \quad (7)$$

According to this model, the temporal profile of the fluorescence should be fitted by a biexponential function. The solid lines in Figure 3b are obtained by the multiexponential fit convoluted with the system response function as

$$I_{fl}(t) = \int dt' \sum_i a_i \exp\left(-\frac{t}{\tau_i}\right) I_{rf}(t - t') \quad (8)$$

where $I_{fl}(t)$ is the intensity of fluorescence at time t, a_j the pre-exponential factor, and τ_j the time constant, respectively. $I_{rf}(t)$ is the system response function determined by the rise profile of the integrated fluorescence intensity of the reference sample (C153 in cyclohexane), where the functional form of the response function was assumed to be

$$I_{rf}(t) \propto \exp\left[-\left(\frac{t - t_0}{\tau_S}\right)^2\right] \quad (9)$$

Here τ_s is the instrumental response time. The response time of the streak camera was dependent on the time range of the measurement (from minimum of ca. 0.02 ns for the 1 ns time window to ca. 0.5 ns for 20 ns time window). As is shown in the figure, there is a very fast decay of ROH*, which was not well resolved within the time resolution of the streak camera. The slower decay component, or RO⁻*, was almost simulated by a single exponential function (the lifetime was 7.4 ns), although a small contribution of another decay (2.3 ns) existed. The decay of ROH* was also simulated by the same time constants. According to refs 36 and 37, the longer time fluorescence decay
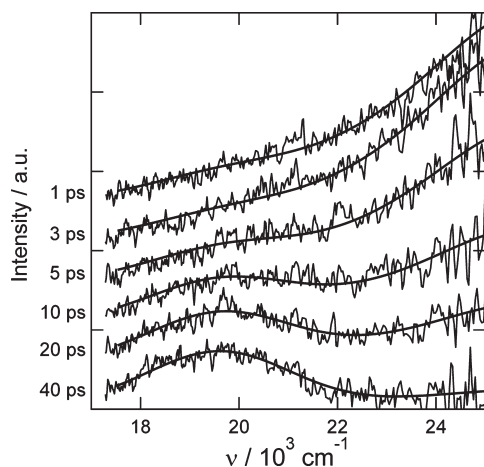
Figure 4. Fluorescence spectra under ambient conditions measured by the optical Kerr gate method. Smooth curves are the fitting results obtained with two log−normal functions. Each spectrum at a different delay time is shown with a different vertical offset.
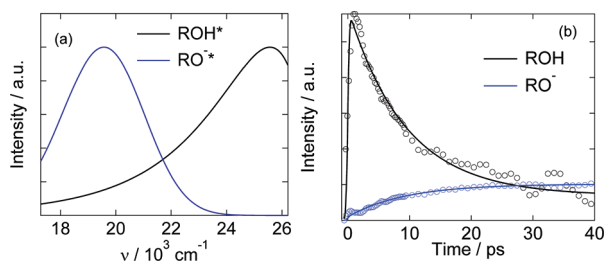
Figure 5. (a) Spectral components and (b) their time profiles under ambient conditions obtained by fitting the sum of two log−normal functions to the data. In panel b, the solid lines represent the fitting curves of the exponential function convoluted with the response function to the time profiles.

of RO⁻* was not exponential, but simulated by a function of $t^{-3/2}$ due to the effect of the backward diffusion-limited reaction. The apparent biexponential decay may be due to the nonexponential nature of the kinetics. Almost similar time profiles were obtained for the data at room temperature and 39 MPa.

To determine the time constant of the fast PT process, the fluorescence spectra detected by the optical Kerr gate method (Figure 4) were analyzed, where the system response function was ca. 0.4 ps. As was done in the preceding paragraph, the spectrum was simulated by two log−normal functions, resulting in the smooth curve lines in Figure 4. The spectral components and their time profiles are given in panels a and b, respectively, of Figure 5. Because our Kerr system had very low sensitivity in the wavelength range below 400 nm, the evaluation of the exact spectral profile for ROH* was not very successful; that is, the sensitivity corrections using standard dyes still have uncertainty in the lower-wavelength region (or the higher-wavenumber region), and therefore the spectral shapes obtained by the Kerr gate measurement did not coincide with those determined by the streak camera. However the spectra of ROH* and RO⁻* were well separated, and each time profile was well extracted. By a simultaneous fit of the time profiles with the same time constant, the fast decay (ROH*) and rise (RO⁻*) times, which correspond to k_1^{-1} (eq 6), was estimated to be 8.2 ps.
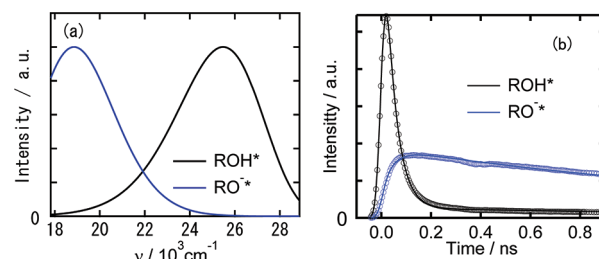
Figure 6. (a) Spectral components and (b) their time profiles at 519 K and 39 MPa obtained by fitting the sum of two log−normal functions to the data. In panel b, the solid lines represent the fitting curves of the exponential function convoluted with the response function to the time profiles.

At the elevated temperatures to 567 K under 39 MPa, almost similar fluorescence dynamics was observed, although the PT kinetics became slower. An example of the spectral decomposition is shown in Figure 6 (the fitting examples are shown in Figure 2b). The fitting results for the streak camera are summarized in Tables 1 and 2.

3.2.3. Fluorescence Dynamics from 615 to 664 K at 39 MPa ($\rho_r = 2.13-1.72$). At 615 K and 39 MPa, three components were suggested to exist from the SVD analysis (Figure S1C, Supporting Information). According to the discussion in section 3.2.1, these species were assigned to ROH*, RO⁻*, and X, and we simulated the spectrum at each delay time by the sum of three log−normal functions as follows: First, the fluorescence spectrum at a longer delay time (ca. 1.5 ns) was simulated by two log−normal functions to obtain the parameters (ν_p, γ, and Δ) for RO⁻* and X. Second, the fluorescence spectrum at the initial delay time (ca. 0.05 ns) was simulated by two log−normal functions (ROH* and RO⁻*) only with adjustable parameters for ROH*. Then, the spectrum at each delay time was simulated by the sum of these three log−normal functions with different intensities. Figure 7 shows the spectral components and their time profiles (spectral fitting results obtained using these spectral species are shown in Figure 2c). The spectral component of X was slightly red-shifted with respect to that of ROH*.

In Figure 7b, it is apparent that the initial decay time of ROH* was similar to the rise time of RO⁻* and the faster rise time of X and that the decay time of RO⁻* was similar to the slower rise time of X. On the basis of these observations, the most general reaction scheme assuming that X is produced from both ROH* and RO⁻* is shown in Scheme 1b. Rate equations for this scheme are given in Supporting Information (section S1). However, the general solutions for eqs S-1−S-3 (Supporting Information) are very complicated and useless. Viewing the time profiles shown in Figure 7b, the rise of RO⁻* (k_d) seems to be the faster than the other processes related to ROH* and X (i.e., $k_d \gg k_P[H^+]$, k_f, k_0, $k_f'[H^+]$, k_0'), because the initial decay time of ROH* was similar to the rise time of RO⁻*. The formation of X ($k_f'[H^+]$) seems to be faster than the intrinsic decay processes of RO⁻* and X ($k_f'[H^+] > k_0'$, k_{OX}), because the decay time of RO⁻* was similar to the slower rise time of X. Under these assumptions, the rate equations were approximately solved to give the triexponential function for each species as in eqs S-6, S-9, and S-10 (Supporting Information). In accordance with these equations, each time profile was simulated by triexponential functions with common lifetimes, and the results are shown by the solid lines in Figure 7b. According to eqs S-6, S-9, and S-10 (Supporting Information),

Table 1. Time Constants Estimated by the Convolution Fitting of the Time Profiles of the Fluorescence Intensity of Each Component to a Multi-Exponential Function[a,b]

T (K)	P (MPa)	ρ_r	ε	species	a_1	a_{S2}	a_S	k_1^{-1} (ns)	k_{S2}^{-1} (ns)	k_S^{-1} (ns)	ν_P (10^3 cm^{-1})
295	0.1	3.10	79.5	ROH*	1 ± 0.19	0.06 ± 0.01	0.02 ± 0.01	0.02(f)	2.07 ± 0.07	7.5 ± 0.1	24.8
				RO$^-$*	-0.21 ± 0.01	-0.26 ± 0.01	0.82 ± 0.01				19.1
295	39	3.15	81.0	ROH*	1 ± 0.03	0.05 ± 0.01	0.04 ± 0.01	0.02(f)	2.3 ± 0.06	7.3 ± 0.1	24.5
				RO$^-$*	-0.27 ± 0.23	-0.24 ± 0.03	0.76 ± 0.04				19.1
471	39	2.77	36.6	ROH*	1 ± 0.02	0.06 ± 0.01	0.021 ± 0.01	0.039 ± 0.003	0.25 ± 0.02	2.4 ± 0.1	25.1
				RO$^-$*	-0.20 ± 0.01	0.02 ± 0.01	0.34 ± 0.01				18.8

[a] Amplitude factors were scaled by the maximum value under each set of experimental conditions. [b] (f) indicates that a value was fixed during the fitting procedure.

Table 2. Time Constants Estimated by the Convolution Fitting of the Time Profiles of the Fluorescence Intensity of Each Component to a Multi-Exponential Function for Different Experimental Conditions[a]
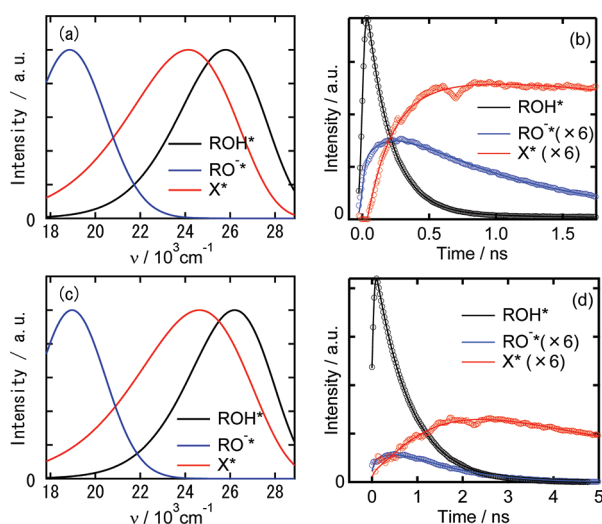
T (K)	P (MPa)	ρ_r	ε	species	a_1	a_S	k_1^{-1} (ns)	k_S^{-1} (ns)	ν_P (10^3 cm^{-1})
519	39	2.60	29.3	ROH*	1 ± 0.01	0.03 ± 0.01	0.042 ± 0.003	1.79 ± 0.01	25.5
				RO$^-$*	-0.12 ± 0.01	0.19 ± 0.01			18.9
567	39	2.40	23.1	ROH*	1 ± 0.07	0.03 ± 0.01	0.078 ± 0.003	1.44 ± 0.07	25.5
				RO$^-$*	-0.15 ± 0.01	0.22 ± 0.01			18.5

[a] Amplitude factors were scaled by the maximum value under each set of experimental conditions.

Figure 7. (a,c) Spectral components and (b,d) their time profiles (a,b) at 615 K and 39 MPa and (c,d) at 664 K and 39 MPa, obtained by fitting the sum of three log—normal functions to the data. In panels b and d, the solid lines represent the fitting curves of the exponential function convoluted with the response function to the time profiles.

the fastest component corresponds to the sum of the rate constants between ROH* and RO$^-$* (k_1)(eq 6), the second fastest component corresponds to the sum of the rates between RO$^-$* and X ($k_2 = k_b' + k_f'[\text{H}^+]$), and the slowest component corresponds to the decay of RO$^-$* and X $\{k_s' = (k_0'k_b' + k_{0X}k_f'[\text{H}^+])/k_2\}$. The parameters obtained by the fit are summarized in Table 3.

At 664 K and 39 MPa, similar spectral dynamics was observed. Although the SVD analysis gave only two meaningful SVs, we found it difficult to simulate the spectral dynamics by the sum of two log—normal functions. Therefore, we simulated the spectrum in the same manner as was done for the data at 615 K and 39 MPa assuming three components, ROH*, RO$^-$*, and X.

The results are shown in Figure 7c,d, and the parameters are summarized in Table 3. Although the time profile in Figure 7d was fit by the triexponential function, the signs of the pre-exponential coefficients did not match the prediction by eqs S-6, S-9, and S-10 (Supporting Information). This is probably because the direct path from ROH* to X becomes effective and the assumption used to derive the equations no longer holds.

3.2.4. Fluorescence Dynamics at 664 K from 31 to 23 MPa ($\rho_r = 1.49-0.47$). At 664 K from 31 to 28 MPa, two components were suggested to exist from the SVD analysis (Figure S1D, Supporting Information); one of the species was ROH*, and the other component was X. In the analysis, the fluorescence spectrum at the initial delay time (ca. 0.3 ns) was initially simulated by a single log—normal function to obtain the parameters (ν_p, γ, and Δ) for ROH*, and the fluorescence spectrum at the longer delay time (ca. 17 ns) was simulated by another single log—normal function to obtain the parameters for X. Then, the spectrum at each delay time was simulated by the sum of these two log—normal functions with different intensities.

The spectral components and their time profiles for 664 K and 28 MPa are shown in Figure 8 (Figure 2d shows the spectral fit at each delay time). The decay of ROH* and the rise of X had a similar time constant. Further, the longer decay constants for the two species were similar to each other. Therefore, we assumed that the reaction scheme is given by Scheme 1c, where k_f and k_b are much greater than k_0 and k_{0X}. Both k_0 and k_{0X} are given by the sum of radiative and nonradiative processes to the ground state. The time profiles of [ROH*] and [X] are given by

$$[\text{ROH*}] = [\text{ROH*}]_0 \frac{k_f}{k_3} \left[\exp(-k_3 t) + \frac{k_b}{k_f} \exp(-k_S'' t) \right]$$

$$(10)$$

$$[\text{X}] = [\text{ROH*}]_0 \frac{k_f}{k_3} [-\exp(-k_3 t) + \exp(-k_S'' t)] \quad (11)$$

Table 3. Time Constants Estimated by the Convolution Fitting of the Time Profiles of the Fluorescence Intensity of Each Component to a Multi-Exponential Function for Different Experimental Conditions[a]

T (K)	P (MPa)	ρ_r	ε	species	a_1	a_2	a'_S	k_1^{-1} (ns)	k_2^{-1} (ns)	k'_S^{-1} (ns)	ν_P (10^3 cm^{-1})
615	39	2.13	17.4	ROH*	1 ± 0.01	0.02 ± 0.01	0.01 ± 0.01	0.18 ± 0.01	1.03 ± 0.04	5.3 ± 0.1	25.8
				X	-0.10 ± 0.01	-0.05 ± 0.01	0.13 ± 0.01				24.1
				RO$^-$*	-0.04 ± 0.01	0.08 ± 0.01	0.00 ± 0.01				18.9
664	39	1.72	11.4	ROH*	0.12 ± 0.22	1 ± 0.21	-0.01 ± 0.01	0.68 ± 0.04	0.78 ± 0.03	5.0 ± 0.3	26.2
				X	0.35 ± 0.22	-0.44 ± 0.21	0.09 ± 0.01				24.6
				RO$^-$*	-0.33 ± 0.19	0.34 ± 0.19	0.00 ± 0.01				18.5

[a] Amplitude factors were scaled by the maximum value under each set of experimental conditions.
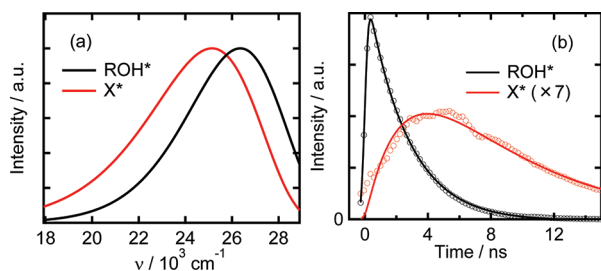
Figure 8. (a) Spectral components and (b) their time profiles at 664 K and 28 MPa obtained by fitting the sum of two log−normal functions to the data. In panel b, the solid lines represent the fitting curves of the exponential function convoluted with the response function to the time profiles.

where

$$k_3 = k_f + k_b \tag{12}$$

$$k''_S = \frac{k_f k_{0X} + k_b k_0}{k_f + k_b} \tag{13}$$

The time profiles for the concentrations of ROH* and X were simulated by biexponential function, and they are shown by the solid lines in Figure 8b. The fitted curves reproduced the observed time profile well, except for the very early dynamics. The obtained parameters are summarized in Table 4.

Finally, for the fluorescence dynamics at 664 K and 23 MPa (ρ_r = 0.47), only one chemical species, ROH*, was suggested to contribute to the fluorescence spectrum from the SVD analysis (Figure S1E, Supporting Information). The spectrum was well fitted by a single log−normal function at any delay time (the peak position of 26800 cm^{-1}), and the decay profile was well simulated by a single exponential function with the lifetime of 4.4 ns.

4. DISCUSSION

The parameters obtained by analyses in section 3 are summarized in Tables 1−4. In the following subsections, we discuss the density dependence of these parameters in relation to the hydrogen-bonding ability and/or the dielectric constant of water.

4.1. Solvatochromic Shifts in Sub- and Supercritical Water. Figure 9 shows the density dependence of the fluorescence peak position of ROH* determined by the spectral fit. The peak position shows a red shift with increasing solvent density, and the dependence is larger in the higher-density region. Although we tried to correlate the spectral shift with the Onsager reaction field, no good linear correlation was found (see Figure S2,

Supporting Information). On the other hand, a nearly linear correlation was found against the value of the dielectric constant (ε), except for the data at ambient temperature (Figure S2, Supporting Information). According to the results of the molecular dynamics simulation, there is a good linear relation between $\varepsilon - 1$ and the number of the hydrogen bonds between water molecules (n_{HB}).[15] Therefore, the apparent relation with ε suggests that the hydrogen bonding between water and 5CN2 is important for the solvatochromic shift.

To examine how water affects the electronic state of the ROH form, we performed DFT calculations on the electronic states of 5CN2 using the 6-31+G(d,p) basis set and the B3PW91 functional implemented in Gaussian 09.[58] Time-dependent DFT was used for the excited-state calculations. We performed structure optimization and vibrational frequency calculations for the several states of 5CN2: an isolated 5CN2, a 1:1 cluster of 5CN2 and water, 5CN2 in polarized continuum model (PCM) water, and 5CN2 in PCM cyclohexane, both in the ground state and in the first excited state. The dipole moment in the ground state (3.71 D) in vapor is similar to that in the excited state (3.95 D), as is consistent with previous calculation results obtained using MCSCF and AM1.[51,59] From this result, it is expected that the spectral shift might not show a correlation with the solvent polarity (or the reaction field). Previously, it was suggested that the local charge distribution of 5CN2 is important for the solvatochromism.[51] In accordance with this prediction, the calculation result for the 1:1 cluster with a water molecule indicates the strong water effect on the transition energy, especially for the hydrogen-bond-donating case of 5CN2 (see Table S1, Supporting Information). Therefore, the local hydrogen bonding surely affects the spectral shift with increasing solvent density from the very low-density region. Of course, the 1:1 cluster calculation exaggerates the water effect of the real system at high temperatures. Further, the transition energy of 5CN2 in the dielectric continuum model of water (results in Table S1, Supporting Information) also showed a red shift of the fluorescence (ca. 1700 cm^{-1}) relative to the value in the vapor, indicating that the dielectric property of water has a non-negligible effect on the transition energy. According to the levels of the present calculations, the combination of the local effect and dipolarity effect is concluded to be the origin of the spectral shift, and more detailed investigation will be required.

The calculations on RO$^-$* (Table S2, Supporting Information) indicate that the fluorescence peak of RO$^-$* shows a blue shift with increasing polarity of the solvent or attaching the water molecule, although the experimentally estimated peak was apparently not dependent on the solvent density. Experimentally, the peak positions of RO$^-$* were estimated less accurately for the following two reasons: First, the signal-to-noise ratio of

Table 4. Time Constants Estimated by the Convolution Fitting of the Time Profiles of the Fluorescence Intensity of Each Component to a Multi-Exponential Function for Different Experimental Conditions[a]

T (K)	P (MPa)	ρ_r	ε	species	a_1	a''_S	k_3^{-1} (ns)	$k''_S{}^{-1}$ (ns)	ν_P (10^3 cm^{-1})
664	31	1.49	9.2	ROH*	1 ± 0.01	−0.021 ± 0.01	1.60 ± 0.03	6.7 ± 0.3	26.3
				X	−0.16 ± 0.01	0.16 ± 0.01			24.9
664	28	1.26	7.2	ROH*	1 ± 0.01	−0.07 ± 0.01	2.67 ± 0.03	6.2 ± 0.2	26.4
				X	−0.20 ± 0.01	0.20 ± 0.01			25.1
664	23	0.47	2.3	ROH*	1			4.4 ± 0.1	26.8

[a] Amplitude factors were scaled by the maximum value under each set of experimental conditions.
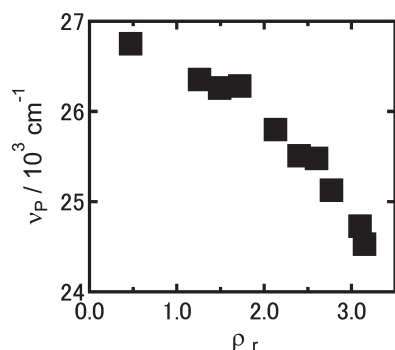
Figure 9. Dependence of the peak position of ROH* fluorescence on the solvent density.
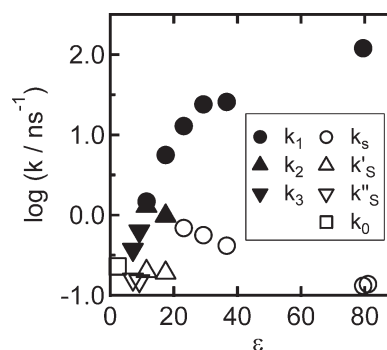
Figure 10. Rate constants plotted against the dielectric constant of water.

the data was too small for accurate analysis, because of the small contribution of RO^{-}* at the higher temperature and the lower density; second, the spectrum of RO^{-}* is quite broad and it was very difficult to estimate the peak position accurately. Therefore, we will not discuss the spectral shift of RO^{-}* further more in this article.

4.2. State-Dependent Proton-Transfer Kinetics in Sub- and Supercritical Water. According to the analysis in section 3, the reaction scheme of 5CN2 upon photoexcitation is strongly dependent on the temperature and the pressure (see Scheme 1), and new chemical species X appears in the intermediate density region. Now a question is what is X. In refs 32 and 33, the formation of a contact ion pair (CIP) of 2-naphtholate anion and a proton was proposed, and it was reported that the emission of CIP was red-shifted to that of 2-naphthol in neutral form. CIP of a proton or $H_5O_2{}^+$ with 5CN2 anion was also proposed in ref 48. These results suggest a possibility that X is a CIP of 5CN2 in the anion form with a proton or protonated water clusters, that is, [RO^{-}···H$^+$], [RO^{-}···$H_3{}^+$O] or [RO^{-}···$H_5{}^+O_2$], etc. We examined the possibility that CIP of RO^{-}* and H_3O^+ can exist by the DFT calculation. At first we have searched a stable structure of the complex RO^{-} (in the ground state) and H_3O^+ starting from arbitrary initial positions in vapor, in PCM water or in PCM cyclohexane. Almost all calculations resulted in the recombination of the proton to RO^{-} and the formation of ROH and H_2O complex. We could find only one structure of CIP in the ground state shown in Figure S3 (Supporting Information), where the proton is situated between water and CN site of 5CN2 in the PCM water and cyclohexane. The stabilization energy is larger in cyclohexane than in water, because CIP is expected to be more stabilized in less polar solvent. It is probable that CIP exists due to the lower dielectric constant of SCW. However, this result is obtained for the ground state, not for the excited state, and cannot be the direct evidence for the existence of CIP in the

excited state. We tried to optimize the excited-state structure starting from the structure in Figure S3 (Supporting Information), but the calculation did not converge. More elaborate theoretical approach including the solvent effect such as reference interaction site model (RISM) SCF is necessary to elucidate the state of X.

By assuming that X is CIP, the variation of the reaction scheme with changing solvent density is explained as follows (Figure 10): From ambient conditions ($\varepsilon = 80$) to 567 K and 39 MPa ($\varepsilon = 23$) with increasing solvent temperature (decreasing density), the PT rate from ROH* to RO^{-}* (k_1) decreased, and simultaneously the lifetime of RO^{-}* (k_S) became short. These changes can be explained by destabilization of the charged species with decreasing dielectric constant and hydrogen-bonding ability and also by the acceleration of the recombination process of the proton to RO^{-}* due to the larger diffusivities of the molecules. Around the density range of $\rho_r = 2.13-1.72$ ($\varepsilon = 17.4-11.4$), the formation rate of CIP from RO^{-}* (k_2) or from ROH* (k_3) becomes comparable to the RO^{-}* formation rate (k_1). (See Table 3.) With a further decrease of the solvent density $\rho_r = 1.49$ ($\varepsilon = 9.2$), the RO^{-}* state is not longer as stable as ROH* anymore, because only the formation of CIP (k_3) occurs. With decreasing density, the formation of the CIP state is suppressed, and at the point of $\rho_r = 0.47$ ($\varepsilon = 2.3$), the decay of ROH* becomes faster than CIP formation, and only the fluorescence from ROH* is observed.

It is interesting to see how this change in the reaction mechanism is related to the solvent polarity or the degree of the hydrogen bonding between solvent molecules. As shown in Figure 10, the crossover of the reaction path occurs around $\varepsilon = 17.4-11.4$, where the number of hydrogen bonds between solvent molecules is around 0.4−0.6 according to the results of MD simulations.[15] The question is how the solute−solvent hydrogen bonding under such conditions is established. Although no direct measurement for 5CN2 in SCW, the previous

Raman study on pNA has important information related to this point.[29] According to the Raman study, the number of hydrogen bonds between NH_2 groups of pNA and ethanol or methanol shows a similar density dependence to that between solvent, and the former dependence is larger than the latter in the medium density region where the number of hydrogen-bonding is close to 0.6. The value is close to that at which the reaction mechanism of PT of 5CN2 changes. Therefore, the hydrogen bonding between 5CN2 and water is expected to exist under the present experimental conditions where the mechanism switching occurs.

It should be noted here that 8−10 water molecules are required for PT under the supersonic jet conditions.[51] DFT calculation results indicate that one water molecule might be enough to form a hydrogen-bonding between water and 5CN2 as is shown in the Supporting Information (Tables S1 and S2). Therefore, the cluster experiments suggest that not only direct hydrogen bonding between 5CN2 and water but also the hydrogen-bonding environment of water molecules are important for PT and that 8−10 water molecules are required to keep the hydrogen-bonding environment for the PT reaction. In our experiment, the crossover of the reaction mechanism occurs in the density region where the number of solvent−solvent hydrogen bonds is 0.4−0.6. Under such conditions, water molecules keep the hydrogen-bonding network environment in part and not isolated. In this sense, our experimental results are consistent with the cluster experiment. More importantly, the available kinetic energy for the reaction is quite large at high temperatures, which makes a large contrast to jet-cooled conditions. The larger available energy makes PT easier to occur in less hydrogen-bonded conditions. More detailed discussion might be possible, if one obtained information on solute−solvent hydrogen bonding between 5CN2 and water in SCW by experiments (e.g., Raman spectroscopy) or simulations in the near future.

5. CONCLUSIONS

In this work, we have investigated the PT process of 5CN2 in water under sub- and supercritical conditions. The PT process of 5CN2 is strongly dependent on the state of water. At 39 MPa from room temperature to 615 K, the fast PT process from 5CN2 became slower. At 615 K and 39 MPa, CIP appeared from RO^{-*} and/or ROH^*. With decreasing density at 664 K, the reaction path to RO^{-*} was hindered, and ROH^* and CIP became major contributors to the fluorescence dynamics. In the very low density region, only the fluorescence from ROH^* was detected. Comparing the reaction with the dielectric constant or the number of hydrogen bonds between water molecules, our experimental results suggest that no PT from 5CN2 to water occurs (no detectable RO^{-*} is formed) below 0.4 of the number of solvent−solvent hydrogen bonds. The proton dissociation rate from 5CN2 to water is significantly increased with increasing number of solvent−solvent hydrogen bonds.

■ ASSOCIATED CONTENT

ⓢ **Supporting Information.** Spectral components and their time profiles obtained by SVD analysis, correlations of fluorescence peak shifts with Onsager reaction fields and dielectric constants, results of the electronic-state calculations of 5CN2 and its anion form in the vapor, in PCM water, and in PCM cyclohexane and of the stable 1:1 cluster with water molecules obtained by DFT calculations, and the stable CIP structure obtained by DFT calculations. This material is available free of charge via the Internet at http://pubs.acs.org.

■ AUTHOR INFORMATION

Corresponding Author
*E-mail: ykimura@kuchem.kyoto-u.ac.jp. Tel.: 075-753-4024. Fax: 075-753-4000.

■ REFERENCES

(1) Weingärtner, H.; Franck, E. U. *Angew. Chem., Int. Ed.* **2005**, *44*, 2672–2692.
(2) Watanabe, M.; Sato, T.; Inomata, H.; Smith, R. L., Jr.; Arai, K.; Kruse, A.; Dinjus, E. *Chem. Rev.* **2004**, *104*, 5803–5821.
(3) Yamaguchi, T.; Yoshida, K.; Yamamoto, N.; Hosokawa, S.; Inui, M.; Baron, A. Q. R.; Tsutsui, S. *J. Phys. Chem. Solids* **2005**, *66*, 2246–2249.
(4) Yamaguchi, T.; Benmore, C. J.; Soper, A. K. *J. Chem. Phys.* **2000**, *112*, 8976–8987.
(5) Matubayasi, N.; Wakai, C.; Nakahara, M. *J. Chem. Phys.* **1997**, *107*, 9133–9140. **1999**, *110*, 8000–8011.
(6) Matubayasi, N.; Nakao, N.; Nakahara, M. *J. Chem. Phys.* **2001**, *114*, 4107–4115.
(7) Hoffmann, M. M.; Conradi, M. S. *J. Am. Chem. Soc.* **1997**, *119*, 3811–3817.
(8) Hoffmann, M. M.; Conradi, M. S. *J. Phys. Chem. B* **1998**, *102*, 263–271.
(9) Tassaing, T.; Danten, Y.; Besnard, M. *J. Mol. Liq.* **2002**, *101*, 149–158.
(10) Lalanne, P.; Andanson, J. M.; Soetens, J. C.; Tassaing, T.; Danten, Y.; Besnard, M. *J. Phys. Chem. A* **2004**, *108*, 3902–3909.
(11) Ikushima, Y.; Hatakeda, K.; Saito, N.; Arai, K. *J. Chem. Phys.* **1998**, *108*, 5855–5860.
(12) Asahi, N.; Nakahara, M. *Chem. Phys. Lett.* **1998**, *290*, 63–67.
(13) Asahi, N.; Nakahara, M. *J. Chem. Phys.* **1998**, *109*, 9879–9877.
(14) Marti, J. *Phys. Rev. E* **2000**, *61*, 449–456.
(15) Yoshii, N.; Miura, S.; Okazaki, S. *Chem. Phys. Lett.* **2001**, *345*, 195–200.
(16) Bennett, G. E.; Johnston, K. P. *J. Phys. Chem.* **1994**, *98*, 441–447.
(17) Xiang, T.; Johnston, K. P. *J. Phys. Chem.* **1994**, *98*, 7915–7922.
(18) Blugarevich, D. S.; Sako, T.; Sugeta, T.; Ohtake., K.; Takebayashi, Y.; Kamizawa, C. *J. Chem. Phys.* **1999**, *111*, 4239–4250.
(19) Lu, J; Boughner, E. C.; Liotta, C. L.; Eckert, C. A. *Fluid Phase Equilib.* **2002**, *198*, 37–49.
(20) Osada, M.; Toyoshima, K.; Mizutani, T.; Minami, K.; Watanabe, M.; Adschiri, T.; Arai, K. *J. Chem. Phys.* **2003**, *118*, 4573–4577.
(21) Oka, H.; Kajimoto, O. *Phys. Chem. Chem. Phys.* **2003**, *5*, 2535–2540.
(22) Kometani, N.; Takemiya, K.; Yonezawa, Y.; Amita, F.; Kajimoto, O. *Chem. Phys. Lett.* **2004**, *394*, 85–89.
(23) Aizawa, T.; Kanakubo, M.; Hiejima, Y.; Ikushima, Y; Smith, R. L., Jr. *J. Phys. Chem. A* **2005**, *109*, 7353–7358.
(24) Minami, K.; Mizuta, M.; Suzuki, M.; Aizawa, T.; Arai, K. *Phys. Chem. Chem. Phys.* **2006**, *8*, 2257–2264.
(25) Mikami, K.; Ohashi, T.; Suzuki, M.; Aizawa, T.; Adshjiri, T.; Arai, T. *Anal. Sci.* **2006**, *22*, 1417–1423.
(26) Fujisawa, T.; Maru, E.; Amita, F.; Harada, M.; Uruga, T.; Kimura, Y. In *Water, Steam, and Aqueous Solutions for Electric Power: Advances in Science and Technology. Proceedings of the 14th International*

Conference on the Properties of Water and Steam; Nakahara, M., Matubayasi, N., Ueno, M., Yasuoka, K., Watanabe, K., Eds.; Japan Society for the Promotion of Science: Tokyo, Japan, 2004; pp 445−450.

(27) Kimura, Y.; Amita, F.; Fujisawa, T. *Rev. High Pressure Sci. Technol.* **2006**, *16*, 87–94.

(28) Fujisawa, T.; Terazima, M.; Kimura, Y.; Maroncelli, M. *Chem. Phys. Lett.* **2006**, *430*, 303–308.

(29) Fujisawa, T.; Terazima, M.; Kimura, Y. *J. Phys. Chem. A* **2008**, *112*, 5515–5526.

(30) Osawa, K.; Hamamoto, T.; Fujisawa, T.; Terazima, M.; Sato, H.; Kimura, Y. *J. Phys. Chem. A* **2009**, *113*, 3143–3154.

(31) Osawa, K.; Fujisawa, T.; Terazima, M.; Kimura, Y. *J. Phys. Conf. Ser.* **2010**, *215*, 012092(4).

(32) Green, S.; Xiang, T.; Johnston, K. P.; Fox, M. A. *J. Phys. Chem.* **1995**, *99*, 13787–13795.

(33) Ryan, E. T.; Xiang, T.; Johnston, K. P.; Fox, M. A. *J. Phys. Chem.* **1996**, *100*, 9395–9402.

(34) Tolbert, L. M.; Haubrich, J. E. *J. Am. Chem. Soc.* **1990**, *112*, 8163–8165.

(35) Tolbert, L. M.; Haubrich, J. E. *J. Am. Chem. Soc.* **1994**, *116*, 10593–10600.

(36) Huppert, D.; Tolbert, L. M.; Linares-Samaniego, S. *J. Phys. Chem. A* **1997**, *101*, 4602–4605.

(37) Solntsev, K. M.; Huppert, D.; Agmon, N. *J. Phys. Chem. A* **1999**, *103*, 6984–6997.

(38) Solntsev, K. M.; Huppert, D.; Agmon, N.; Tolbert, L. M. *J. Phys. Chem. A* **2000**, *104*, 4658–4669.

(39) Cohen, B.; Huppert, D. *J. Phys. Chem. A* **2000**, *104*, 2663–2667.

(40) Cohen, B.; Huppert, D. *J. Phys. Chem. A* **2001**, *105*, 2980–2988.

(41) Cohen, B.; Segal, J.; Huppert, D. *J. Phys. Chem. A* **2002**, *106*, 7462–7467.

(42) Cohen, B.; Leiderman, P.; Huppert, D. *J. Phys. Chem. A* **2003**, *107*, 1433–1440.

(43) Koifman, N.; Cohen, B.; Huppert, D. *J. Phys. Chem. A* **2002**, *106*, 4336–4334.

(44) Genosar, L.; Leiderman, P.; Koifman, N.; Huppert, D. *J. Phys. Chem. A* **2004**, *108*, 309–319.

(45) Genosar, L.; Lasitza, T.; Gepshtein, R.; Leiderman, P.; Koifman, N.; Huppert, D. *J. Phys. Chem. A* **2005**, *109*, 4852–4861.

(46) Gopich, I. V.; Solntsev, K. M.; Agmon, N. *J. Chem. Phys.* **1999**, *110*, 2164–2174.

(47) Solntsev, K. M.; Agmon, N. *Chem. Phys. Lett.* **2000**, *320*, 262–268.

(48) Barroso, M.; Arnaut, L. G.; Formosinho, S. J. *J. Photochem. Photobiol. A* **2002**, *154*, 13–21.

(49) Tomasko, D. L.; Knutson, B. L.; Pouillot, F.; Liotta, C. L.; Eckert, C. A. *J. Phys. Chem.* **1993**, *97*, 11823–11834.

(50) Nunes, R. M. D.; Arnaut, L. G.; Solntsev, K. M.; Tolbert, L. M.; Formosinho, S. J. *J. Am. Chem. Soc.* **2005**, *127*, 11890–11891.

(51) Knochenmuss, R.; Solntsev, K. M.; Tolbert, L. M. *J. Phys. Chem. A* **2001**, *105*, 6393–6401.

(52) Jacobs, S. A.; Harvey, R. G. *J. Org. Chem.* **1983**, *48*, 5134–5135.

(53) Kimura, Y.; Fukuda, M.; Suda, K.; Terazima, M. *J. Phys. Chem. B* **2010**, *114*, 11847–11858.

(54) Wagner, W.; Kruse, A. *Properties of Water and Steam*; Springer-Verlag: Berlin, 1998.

(55) See, for example: Park, S.; Moilanen, D. E.; Fayer, M. D. *J. Phys. Chem. B* **2008**, *112*, 5279–5290.

(56) Michael, E. W.; Rechtsteiner, A.; Rocha., L. M. In *A Practical Approach to Microarray Data Analysis*; Berrar, D.P., Dubitzky, W., Granzow, M., Eds.; Kluwer: Norwell, MA, 2003; pp 91−109.

(57) Swinney, T. C.; Kelley, D. F. *J. Chem. Phys.* **1993**, *99*, 211–221.

(58) Frisch, M. J.; Trucks, G. W.; Schlegel, H. B.; Scuseria, G. E.; Robb, M. A.; Cheeseman, J. R.; Scalmani, G.; Barone, V.; Mennucci, B.; Petersson, G. A.; Nakatsuji, H.; Caricato, M.; Li, X.; Hratchian, H. P.; Izmaylov, A. F.; Bloino, J.; Zheng, G.; Sonnenberg, J. L.; Hada, M.; Ehara, M.; Toyota, K.; Fukuda, R.; Hasegawa, J.; Ishida, M.; Nakajima, T.; Honda, Y.; Kitao, O.; Nakai, H.; Vreven, T.; Montgomery, J. A., Jr.; Peralta, J. E.; Ogliaro, F.; Bearpark, M.; Heyd, J. J.; Brothers, E.; Kudin, K. N.; Staroverov, V. N.; Kobayashi, R.; Normand, J.; Raghavachari, K.; Rendell, A.; Burant, J. C.; Iyengar, S. S.; Tomasi, J.; Cossi, M.; Rega, N. ; Millam, J. M.; Klene, M.; Knox, J. E.; Cross, J. B.; Bakken, V.; Adamo, C; Jaramillo, J.; Gomperts, R. E.; Stratmann, O.; Yazyev, A. J.; Austin, R.; Cammi, C.; Pomelli, J. W.; Ochterski, R.; Martin, R. L.; Morokuma, K.; Zakrzewski, V. G.; Voth, G. A.; Salvador, P.; Dannenberg, J. J.; Dapprich, S.; Daniels, A. D.; Farkas, O.; Foresman, J. B.; Ortiz, J. V.; Cioslowski, J.; Fox, D. J. *Gaussian 09*, revision A.1; Gaussian, Inc.: Wallingford C,T, 2009.

(59) Agmon, N.; Rettig, W.; Groth, C. *J. Am. Chem. Soc.* **2002**, *124*, 1089–1096.